NeuroRoots, a bio-inspired, seamless brain machine interface for long-term recording in delicate brain regions

Cite as: AIP Advances 14, 085109 (2024); doi: 10.1063/5.0216979
Submitted: 2 May 2024 • Accepted: 9 July 2024 •
Published Online: 7 August 2024

Marc D. Ferro,[1] Christopher M. Proctor,[2] Alexander Gonzalez,[3] Sriram Jayabal,[3] Eric Zhao,[1] Maxwell Gagnon,[3] Andrea Slézia,[4] Jolien Pas,[5] Gerwin Dijk,[5] Mary J. Donahue,[6] Adam Williamson,[7,8] Jennifer Raymond,[3] George G. Malliaras,[2] Lisa Giocomo,[3] and Nicholas A. Melosh[1,a)]

AFFILIATIONS

[1] Department of Materials Science and Engineering, Stanford University, Stanford, California 94305, USA
[2] Electrical Engineering Division, Department of Engineering, University of Cambridge, Cambridge CB3 0FA, United Kingdom
[3] Department of Neurobiology, Stanford University School of Medicine, Stanford, California 94304, USA
[4] Multimodal Neurotechnology Group, Institute of Cognitive Neuroscience and Psychology, HUN-REN Research Centre for Natural Sciences, Hungarian Research Network, 1117 Budapest, Magyar tudósok körútja 2., Hungary
[5] Department of Bioelectronics, Ecole Nationale Supérieure des Mines, CMP-EMSE, 13541 Gardanne, France
[6] Laboratory of Organic Electronics, Department of Science and Technology, Linköping University, Norrköping, 60221, Sweden
[7] International Clinical Research Center, ICRC, St. Anne's University Hospital and Faculty of Medicine, Masaryk University, Brno, Czech Republic
[8] Center for Social and Affective Neuroscience, Department of Biomedical and Clinical Sciences, Linköping University, Linköping, Sweden

[a)] **Author to whom correspondence should be addressed:** nmelosh@stanford.edu

ABSTRACT

Scalable electronic brain implants with long-term stability and low biological perturbation are crucial technologies for high-quality brain–machine interfaces that can seamlessly access delicate and hard-to-reach regions of the brain. Here, we created "NeuroRoots," a biomimetic multi-channel implant with similar dimensions (7 μm wide and 1.5 μm thick), mechanical compliance, and spatial distribution as axons in the brain. Unlike planar shank implants, these devices consist of a number of individual electrode "roots," each tendril independent from the other. A simple microscale delivery approach based on commercially available apparatus minimally perturbs existing neural architectures during surgery. NeuroRoots enables high density single unit recording from the cerebellum *in vitro* and *in vivo*. NeuroRoots also reliably recorded action potentials in various brain regions for at least 7 weeks during behavioral experiments in freely-moving rats, without adjustment of electrode position. This minimally invasive axon-like implant design is an important step toward improving the integration and stability of brain–machine interfacing.

INTRODUCTION

Brain machine interfaces (BMIs) are playing an increasingly important role in neurological research,[1–4] clinical treatments,[5,6] and neural-prosthetics.[7–9] With the advent of powerful signal processing and data analytics software, the impetus has shifted from two-dimensional bulky probes to developing electrical implants with higher channel counts, lower tissue damage, and long-term recording stability from a population of neurons, with high resolution even at the single cell level. Previous generations of bulky, stiff electrodes are being replaced by a number of innovative new

devices[10–13] for lowering tissue damage,[14] increasing chronic stability using ultra-flexible meshes,[15–17] flexible arrays[2,18–20] and stretchable electrodes,[3,21] and increasing channel counts.[22–25] However, achieving the optimal combination of low tissue damage, scalability, and non-perturbative surgical implantation remains challenging.

To overcome the limitations of planar designs, we sought inspiration from biological structures and the bundles of myelinated axons in the white matter that coordinate the communication between different brain regions. Here, we present axonal bundle mimics with similar spatial distribution and design to human axons,

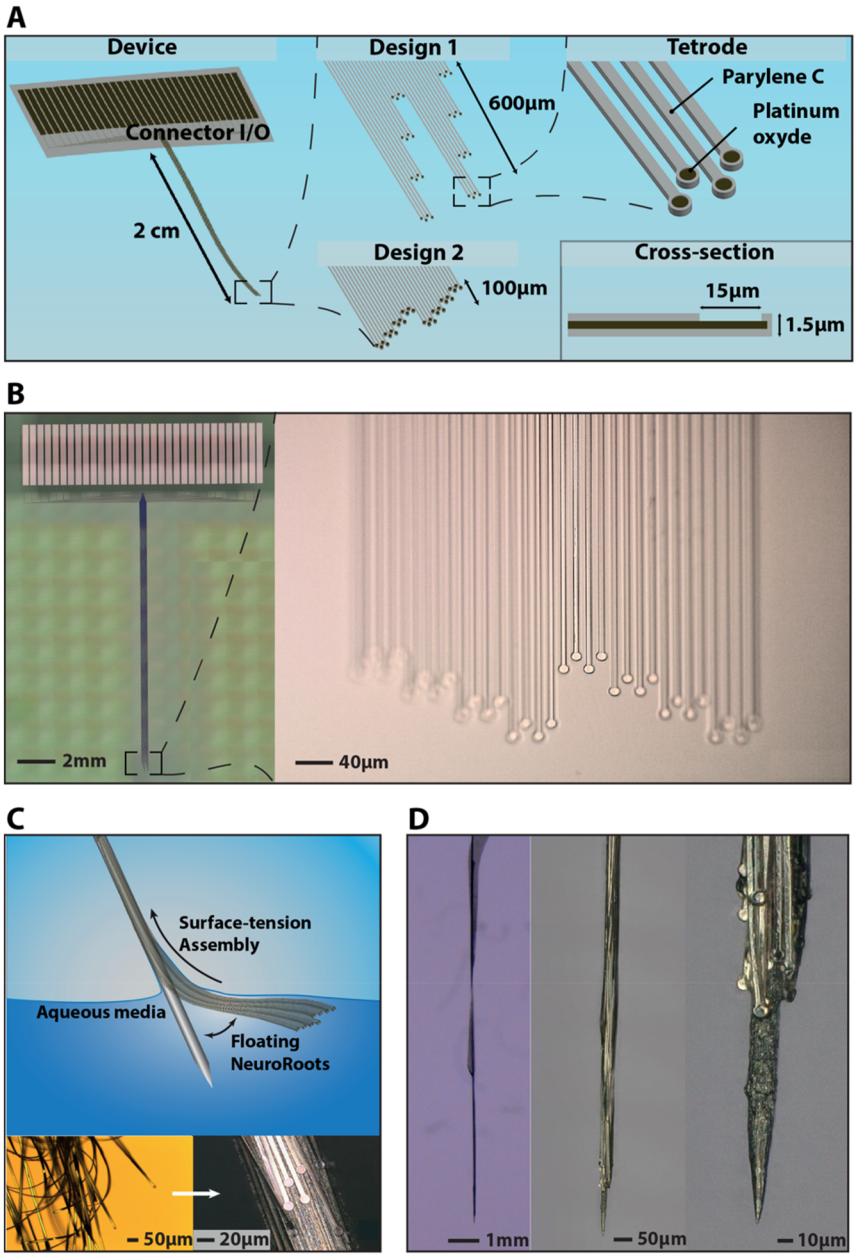

FIG. 1. (a) NeuroRoots overview and assembly. 3D model of the NeuroRoots and the different configurations of the tip. Design 1 and 2 are zoomed-in representations of the tip with the electrodes organized in 150 and 25 μm depth spacing, respectively. A zoomed-in representation of one tetrode-like set of electrodes and the cross-sectional representation are also presented. Parylene C substrate is represented in light gray and platinum in dark brown. (b) Microscope picture image of the NeuroRoots with Design 1 and Design 2. (c) Assembly method using capillary and surface-tension effects to draw the electrodes onto the microwire. Bottom insets show a microscope picture of the electrode leads after delamination from the fabrication substrate and after lamination on a substrate. (d) Microscopy showing the electrodes assembled onto electrosharpened microwires, demonstrating their spacing is set by the initial position in the array.

which range from 0.5 to 9 μm in diameter,[26] can be many centimeters in length, and exhibit elastic moduli of roughly 10 kPa.[27] These "NeuroRoots" [Fig. 1(a)] consist of arrays of individual electrodes, ~7 μm wide, ~1.5 μm thick, yet centimeters long and organized in axon-like tendrils. Each electrode has a single, ~10 μm diameter recording pad at its tip, and is mechanically separate from the other electrodes, allowing complete flexibility in the number of electrodes at a given depth while minimizing the electrode width, and thus damage. This is a significantly different design from arrays of electrodes on a single shank, where the device width must increase to accommodate more electrodes at the same location. Moreover, the electrodes described here have similar mechanical flexibility as myelinated axons, ideally enhancing long-term stability while lowering immunogenicity.

Herein, we present a strategy to manufacture, assemble, and implant these ultra-flexible micro-electrodes. Implantation is one of the key challenges for flexible devices, as they normally are not stiff enough to penetrate tissue. Often, a polymer stiffening agent or shuttle is used; however, these produce large devices that can cause considerable tissue compression and bleeding, despite the functional device being quite small. To avoid this issue, we use capillary assembly of the NeuroRoots onto an ultra-thin microwire as small as 35 μm diameter, which causes very little tissue damage.[28] This simple approach can be used with traditional tetrode surgical apparatus for spatial targeting and data acquisition and allows the implantation of 32 electrodes with a footprint below 40 μm in diameter. Surgeries can be performed through small boreholes rather than full craniotomies and within a reasonable timeframe. NeuroRoots devices provided stable chronic recordings in deep-brain regions of freely-behaving rats with minimal variation in the signal over a period of 7 weeks. In addition, single-units were recorded from the cerebellum both *in vitro* and *in vivo*, which is—to our knowledge—the first report of flexible multielectrode array recordings in this region of the brain.

RESULTS AND DISCUSSION

Fabrication and electrical performance

The design of NeuroRoots [Fig. 1(a)] consists of independent polymer/metal/polymer "roots," with thin leads connecting exposed recording pads at the tips to larger pads at the proximal end that can be further connected to standard acquisition systems. The specific device sizes, number of electrodes, and electrode materials were readily varied using standard photolithography and etching techniques. Parylene-C (PaC), a flexible and biocompatible polymer, was chosen as a substrate and insulator to encapsulate platinum (Pt) film used as a conductive layer. In a typical preparation, the cross-section of the device was measured to be 1.5 μm thick, which includes both layers of PaC (0.75 μm each) and the layer of Pt of 100 μm [Fig. 1(a): cross-section]. The leads were 7 μm wide with 10 or 15 μm circular electrode pads at the end, where a window in the upper PaC layer was opened to expose the bare Pt metal. Parylene C is about 40 times stiffer than a human axon with a Young modulus of 400 kPa, though, because of its geometrical thickness and dimensions, NeuroRoots exhibit a bending stiffness equivalent to a human axon of 3 μm in diameter (Fig. S1).

The electrode configuration was organized into clusters of tetrodes [Fig. 1(a)] and the spatial distribution of the leads could be varied depending on the desired locations of the electrodes in the tissue, as the insertion process preserved the relative position of each electrode. Two different organizations of the 32 electrodes at the tip of the implants were prepared, either distributed over 600 μm [Fig. 1(a): Design 1] or densely packed into a layer of 100 μm in longitudinal depth [Fig. 1(a): Design 2]. In an alternative design, the electrodes were coated with poly(3,4-ethylenedioxythiophene)-poly(styrene sulfonate) (PEDOT:PSS) and had a rectangular shape with a width of the lead and a length up to 100 μm (Fig. S2). Importantly, unlike conventional shank electrodes, the NeuroRoots recording pad distribution does not have to be uniform and could for instance have several regions of ultra-dense sampling up to ~5× the current state-of-the-art,[22] or a sparse sampling over large distances. This could be advantageous for studying local neural architecture[29,30] or dynamics and plasticity in behaving animals under different brain or behavioral states.[31]

The rough Pt or PEDOT-PSS pads at each tip provided low impedance electrodes. For example, the 15 μm diameter Pt electrodes exhibited an average impedance of 40 kΩ at 1 kHz, that is, a specific impedance of 55 Ω μm (Fig. S3). This is more than an order of magnitude lower than the impedance of smooth noble metal electrodes and comparable to electrodes of similar surface-area coated with a thin layer of PEDOT:PSS.[32] As a direct comparison, a typical wire used in a tetrode exhibits the same electrode surface area but an average impedance of 300 kΩ.

Assembly

A critical challenge for these and other very soft electrodes is insertion into the brain due to their fragility and lack of mechanical stiffness. Previous research has shown that compliant electrodes can be inserted using mechanical shuttles,[33] stiffening agents,[34,35] or syringes.[16] However, standard shuttles for a planar array of the NeuroRoots would be hundreds of micrometers wide and cause significant damage. Instead, we developed an electrode self-assembly method using capillarity to organize large arrays of NeuroRoots onto a microwire as small as 35 μm in diameter, which in turn provides mechanical support to allow implantation, yet with minimal damage.[36,37]

A capillary assembly method controllably immobilized the roots over the surface of the microwire with the same vertical distribution as the original lithographic pattern [Fig. 1(b)]. First, NeuroRoots were soaked in deionized (DI) water following the microfabrication process, allowing the implant to detach from the substrate [Fig. 1(c)]. PaC exhibits a high interfacial energy with water,[38] which allowed the film to unfold and float at the air/liquid interface in its initial configuration. Second, a tungsten microwire was brought into contact with the implant at an ~45° angle, and floating electrodes were lifted by allowing surface tension to draw the NeuroRoots onto the microwire surface while being withdrawn from the liquid [Fig. 1(c)]. By capillarity, a small amount of aqueous solution would coat the microwire and offer a preferred energetic solution. Note that these floating electrodes could be transferred onto a variety of materials and devices, including flexible plastics, glass optical-fiber, or shaped silicon if desired.[39] Critically, capillary forces and surface tension directed all of the individual leads of the NeuroRoots to self-assemble onto the microwire, despite the leads initially spanning nearly ten times the width of the microwire [Fig. 1(c)]. The floating electrodes were handled by the connector

I/O, which avoided damaging the roots themselves and offered a macroscopic handle for the implant.

In order to allow the NeuroRoots to controllably desorb from the microelectrode after implantation, we included a small concentration of bio-soluble, inert polymer in the capillary assembly solution. We found that using a mixture of low molecular weight polyethylene glycol (PEG) in DI water could provide a release time frame between 2 and 10 min, depending on the PEG concentration. To minimize the device footprint, we used microwires as small as 35 μm diameter and electro-sharpened the tip down to a few 100 nm [Fig. 1(d)]. Once assembled, the electrode bundle cross-section was measured to ~38 μm, which is less than the size of a single tetrode, yet with eight times the recording capacity, and less than half the size of a single Utah array shank (80 μm in diameter[40]), a Michigan standard probe (125–50 μm[41]), or even the ultra-thin silicon Neuropixel probe (70 μm wide × 20 μm thick[22]).

Implantation

The NeuroRoots were then implanted using standard surgical apparatus developed for tetrode devices, which often use wire electrodes. A borehole of ~2 mm^2 in size was prepared and the electrodes were inserted at a speed of ~1.5 mm/s. Once inserted into the region of interest, the microwire was retracted [Fig. 2(b)], leaving the roots distributed according to their original length [Fig. 2(d)]. In addition, X-ray microtomography (μCT) was used to image larger devices (100 μm wide) and validate successful delivery and placement of the NeuroRoots *in vivo* [Fig. 2(c)]. Using this approach, we could accurately implant the electrodes while keeping a surgical footprint as low as 38 μm [Fig. 4(c)], thereby reducing local bleeding, compression, and force necessary to puncture the brain surface, which is crucial to mitigate both initial damage and chronic tissue inflammation.[42] Histology revealed very little activation of microglia and reactive astrocyte around the implants (Fig. S4).

An additional advantage of this implantation strategy is the reduced risk of mechanical failure after insertion compared with rigid implants, which can account for up to 50% of all failure modes.[43] After the microwire removal, the implant was provided with additional mechanical slack by lowering the Z axis of the stereotaxic frame by ~500 μm before sealing the implant to the skull. This allowed for the decoupling of the direct mechanical constraint between the implant and the brain, which is under constant micromotion.[44] Over the course of a total of 12 rodent surgeries, we did not observe any acute or chronic mechanical failure for the NeuroRoots.

Chronic apparatus

The base of a Neuralynx "Halo 18" was used as a starting platform to make the system compatible with commercially available electrophysiology and behavioral rigs, thus minimally impacting the surgery and recording procedures [Fig. 2(a)]. A guide system was engineered to interface the NeuroRoots microelectrode and enable a precise alignment of the microwire, compatible with targeting using the standard stereotaxic approach [Fig. 2(a)]. The NeuroRoots were connected to either an RHS2000 (Intan Technology) or a "EIB 72" (Neuralynx) through a custom-designed Printed Circuit Board (PCB) and a Zero Insertion Force (ZIF) connector. The entire platform was then securely assembled into a 3D-printed scaffold hat with only the tip of the implant protruding. The weight of the final device was measured to be 8 g, which is <2% of an adult rat weight.[7] Our demonstration was done using only 32 channels, which was largely limited by the bulkiness of currently available connectors. As new headstage and connection technologies emerge, the unique form factor of NeuroRoots will allow for scaling up the number of channels to a few hundred without dramatically increasing the implant footprint. For example, a 10-fold increase in channel count (320 electrodes) increases the diameter of the implant by a factor of two (60 μm in diameter), which is still quite small compared to current Michigan or Utah style devices.

Chronic recordings

We demonstrated chronic recording of the NeuroRoots in adult rats, freely moving in a maze equipped with infrared video tracking and automated reward systems [Fig. 3(c)]. We targeted the NeuroRoots into the CA1 region of the hippocampus in both acute and chronic experiments in fully-grown rats. The raw signal exhibited a high signal-to-noise ratio (SNR) of 4.1, which allowed for clear identification of different types of activity and action potentials (APs) across the different channels [Fig. 3(a)]. Adjacent electrodes did not exhibit cross-talk, which validated that the geometry used [Fig. 1(a): Design 1] did not oversample the neural region [Fig. 3(a)]. Recordings exhibited characteristic Local Field Potentials (LFPs) with downstate and spindle (12–16 Hz) characteristics of cortical activity [Fig. 3(a)] as well as putative spikes from pyramidal neurons with an average spike width of 500 μs followed by a long-lasting hyperpolarization [Fig. 3(a)]. APs could be observed within a few minutes after surgery, suggesting that the implantation damage was low enough to preserve spontaneous activity from the pre-existing neural tissue around the probe. This is supported by the short recovery period needed, as sortable APs could be observed on all channels on our first experiment four days post-surgery.

Spike averaging into bins of 1 ms centered around sortable spikes revealed a variety of distinct extracellular spike waveforms spread along 32 channels of NeuroRoots [Fig. 3(b)]. Analysis of these waveforms distinguished between two distinct types of activity: neurons with ~1 ms spikes and 50 μV amplitude [Fig. 3(b)] and interneurons characterized by a short spike width (<1 ms) followed by a shorter hyperpolarization period.

We then evaluated the stability of the electrical coupling of the NeuroRoots with the brain by comparing the APs recorded by the same set of electrodes over a period of 7 weeks without any adjustment of the electrodes or electronics [Fig. 3(b)]. The similarity of APs recorded on the same electrodes suggests that the NeuroRoots formed a stable interface with the surrounding neurons. While the shape of the AP was highly consistent, the absolute magnitude varied slightly from week to week [Fig. 3(b)]. This variation was non-monotonic, sometimes increasing or decreasing over time, suggesting it likely arose from natural remodeling near the neuron.[45]

In order to assess whether these were likely to be the same neurons over time, we performed cell sorting using unsupervised clustering and Principal Component Analysis (PCA) (Fig. S5). The result over the seven weeks showed minimal shifts of the cluster center on the same electrode, equivalent to 0.61 σ between the first and last dates, comparable with previously reported chronic

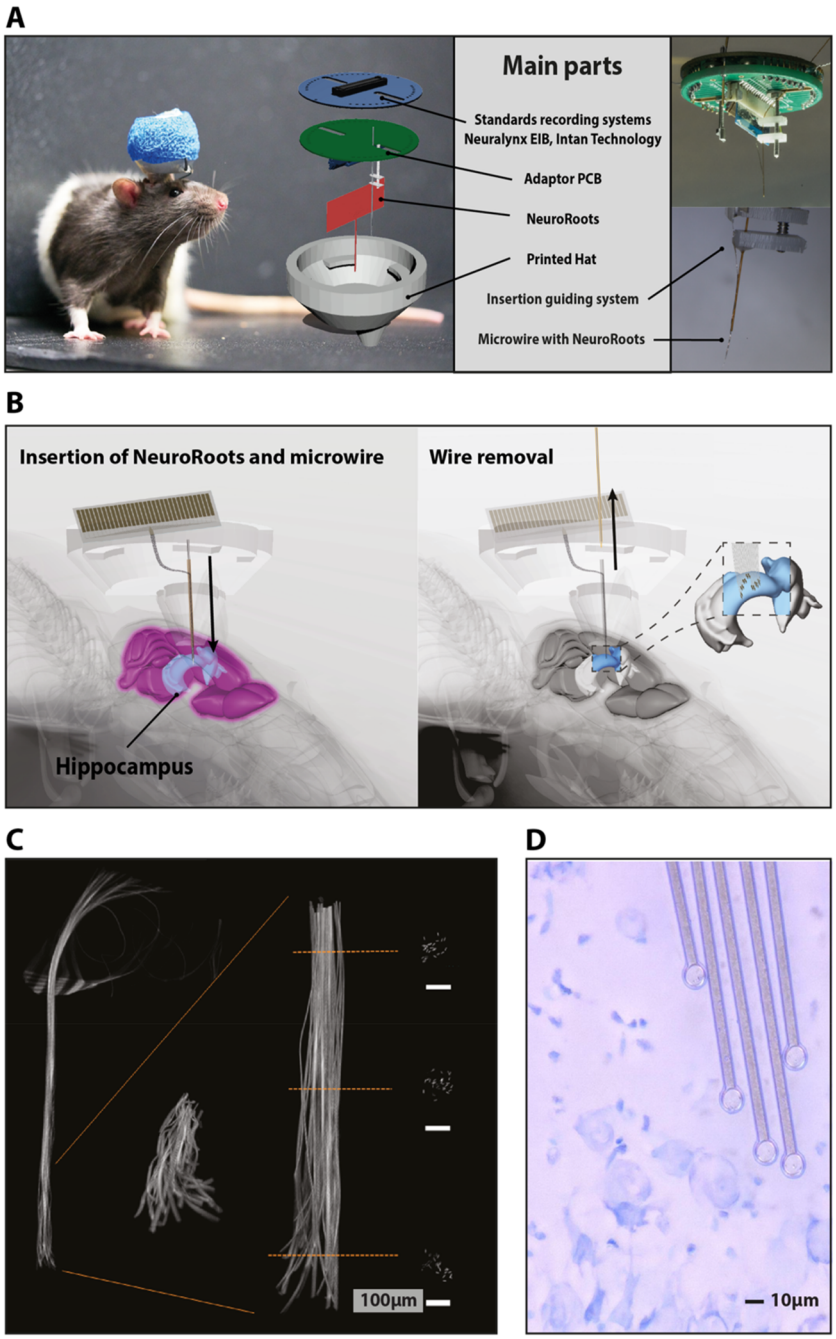

FIG. 2. (a) Apparatus for chronic recordings in freely moving rats. A picture of a rat 4 days post-surgery. The implant connector is protected by a cap on top of the scaffold presented on the right. The 3D exploded-view shows the main parts that compose the NeuroRoots platform. Left pictures show the adaptor and the NeuroRoots assembled before insertion and a zoomed-in picture of the guiding system with the NeuroRoots assembled onto the microwire. (b) Implantation strategy of the NeuroRoots into deep-brain regions. The assembled microwire and NeuroRoots are implanted into the desired brain region through a 3D printed scaffold hat (left). Once the NeuroRoots are released, the microwire is removed, leaving only the electrodes implanted into the brain tissue (right). (c) X-ray microtomography scanning showing the electrode distribution after implantation using PEDOT:PSS based devices. (d) Microscope image of a NeuroRoots placed onto a brain slice of cell CA1 of the hippocampus for scale. The electrodes of 10 μm in diameter are similar in size to neuron soma (Cresyl violet staining).

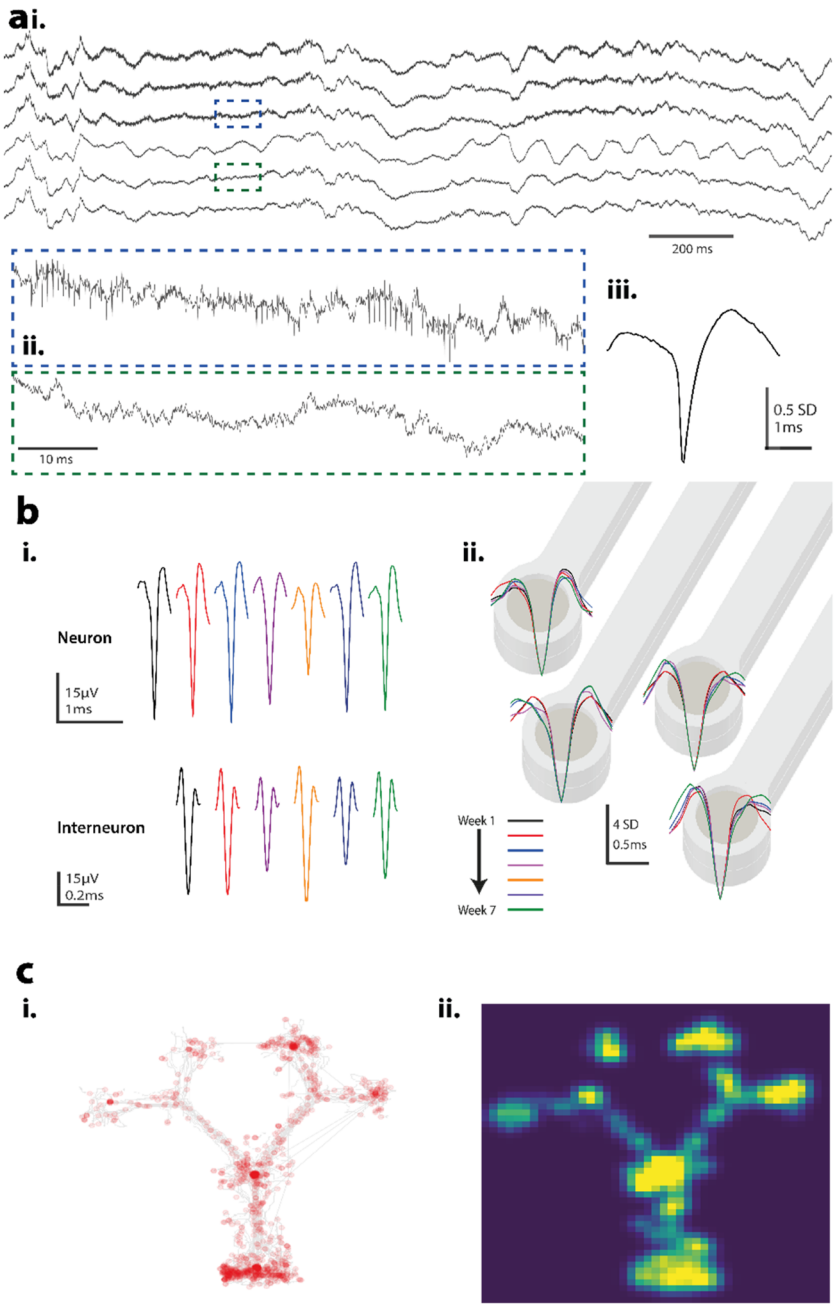

FIG. 3. (a) Representative recordings of raw traces. (i) Two seconds recording of six consecutive channels. Scale: 200 ms. (ii) Zoomed-in view of the blue box presented in (i) shows characteristic activity while the green zoomed-in green box show the activity of a neighbor electrode. Scale: 10 ms. (iii) Action potential of a hippocampal neuron recorded during the acute experiment. Scale: 0.5 SD and 1 ms. (b) Cluster stability assessment during the chronic experiment. (i) Representative APs of the same neuron and interneuron over the 7 weeks of the experiment. Scale neuron: 15 μV, 1 ms, interneuron 15 μV, and 0.2 ms. (ii) Overlay of averaged APs corresponding to a cluster tracked over 7 weeks. Scale: 4 SD and 0.5 ms. Each cluster corresponds to a different electrode. Each color is representative of recordings from a different week as describes in the colored legend. (c) Behavioral analysis. (i) Animal trajectories in gray on a double Y-Maze (1.4 × 1.2 m^2). Spikes from an example cell overlaid in red. (ii) Estimated firing fields for the same cell; warmer color indicates increased firing activity.

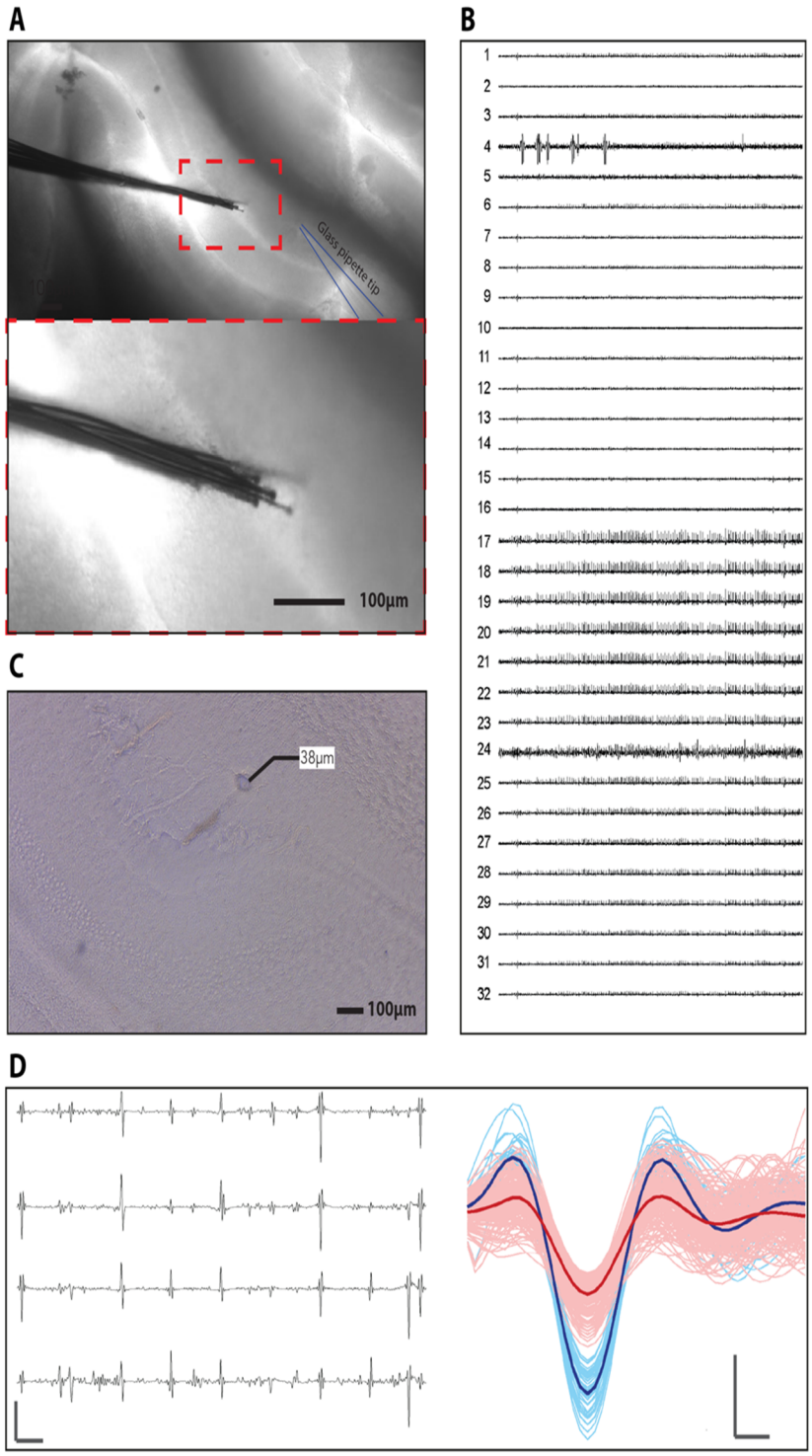

FIG. 4. (a) Microscope image of NeuroRoots implanted into a cerebellar slice. (b) *In vitro* recordings from a cerebellar slice. Typical activity of the 32 channels during recordings. Each trace is (−270; 200] μV and 1 s. (C) Microscope image of the histological slice with the NeuroRoots footprint measured at 38 μm in diameter. (d) *In vivo* recordings in the cerebellum. Typical activity from 4 electrodes after off-line processing, scale bar 100 μV, 4 ms. A typical single unit extracted from one of the channels during *in vivo* recordings is presented on the right. Red and blue colors correspond to two distinct single units and the bold line represents the averaged activity of the spike collected. Scale bar: 200 μV and 0.2 ms.

recordings using ultra-flexible electrodes.[14] Together with the consistent signal shape between the different dates, this suggests that the waveforms were generated by the same neuron. Last, the analysis of the signal-to-noise ratio (SNR) for all 32 channels between the first and the last recording dates showed a remarkable stability, with <3.1% variation around the average. This indicates that the firing neurons remained in close proximity to the electrode for the entire duration, and that the electrode did not undergo any detectable degradation or movement.

We monitored the position of the rat moving within a double Y-Maze and compiled a comparative map of positions vs firing rate [Fig. 3(c)]. Animal trajectories are represented in gray and spikes from an example cell are overlaid in red. Spatial firing fields were estimated for each cell, which allows us to determine if the cell exhibited any spatial selectivity. The maximum firing rate recorded was 1.02 spikes/s, which—although too low to indicate the monitoring of a cell selective for position—demonstrates the compatibility of the NeuroRoots platform with measurements of interest in behavioral experiments.

Recordings in the cerebellum

The cerebellum is an anatomically crystalline, highly multimodal structure, receiving and integrating inputs from multiple sensory modalities.[46] These modalities include vestibular, somatosensory, and visual information for controlling the timing and pattern of muscle activation during movement, which is vital for coordination, dexterity, and maintaining equilibrium,[47] and is therefore important for high-performance neuroprosthetics. Yet the cerebellum's composition of densely packed neurons with high firing rates has made large scale recording from populations of isolated cerebellar neurons challenging. Because of this limitation, most studies have focused on acute recordings of single Purkinje cells using single micro-electrodes, with a few examples of recordings using small arrays of rigid metal or glass electrodes.[48–50] Calcium imaging provides an alternative approach for recording populations of cerebellar neurons;[51–54] however, this method lacks the temporal resolution necessary to analyze the rapid neural dynamics underlying some of the precise motor skills supported by the cerebellum.

After implantation, NeuroRoots were able to successfully record from neurons in the cerebellum in both *in vitro* slice preparations and *in vivo* in anesthetized mice. We first implanted NeuroRoots (Design 2) into a slice, specifically in the lobule IV/V of the cerebellar vermis [Fig. 4(a)] and recorded single units immediately after insertion. The signal quality allowed us to clearly identify and collect spikes on 31 of the 32 channels [Fig. 4(b)]. Furthermore, we implanted NeuroRoots into the cerebellum *in vivo*. Acute recordings show clear spikes of ~1 ms duration and ~200 μV amplitude [Fig. 4(d)]. Further analysis identified distinct APs with ~1 ms duration and amplitudes between ~150 and ~400 μV [Fig. 4(d) and PCA available in Fig. S6].

Histological analysis confirmed the electrode position in the molecular layer as well as the remarkably low footprint measured at 38 μm in diameter after the implant retraction [Fig. 4(c)]. This technology extends the current state-of-the-art[55] by providing a flexible, high-density, and customizable multielectrode array with superior recording resolution. We foresee that by optimizing the electrode density, 3D configuration, and electrode pad size, the NeuroRoots will enable unprecedented sampling of all cerebellar neuronal types, including the granule cell population.

CONCLUSIONS

In this work, we introduce bio-mimetic NeuroRoots electrodes with similar size, flexibility, and distribution as axon bundles in the brain. We demonstrate the implantation of a dense distribution of 32 of these electrodes into the brains of freely moving rats with minimal damage and long-term stable integration within the tissue. Stable neural recordings were made over seven weeks during complex behavioral tasks with freely-moving rats. Moreover, we leverage the NeuroRoots' small footprint and reduced surgical damage to access the cerebellum, one of the densest regions of the brain, demonstrating high quality recordings of single units both *in vitro* and *in vivo*. The combination of scalability, low damage, stable single unit recording, and ready integration with existing surgical and recording equipment makes NeuroRoots a promising candidate for basic neuroscience experiments and clinical applications.

MATERIALS AND METHODS

Probe fabrication and preparation

Fabrication and patterning of PaC and PEDOT:PSS based electrodes were discussed in previous publications.[2,56] In brief, PaC was deposited to a thickness of 1.5 μm (SCS Labcoater 2). A-174 Silane and a dilute solution of industrial cleaner (Micro-90) were used as an adhesion promoter and anti-adhesion, respectively. The film was patterned using a 150 nm thick layer of germanium and dry etched by a plasma reactive-ion etching process (500 W, 50 SCCM O_2, for 5 min) (P5000 etcher), followed by an immersion into deionized water in order to dissolve the metallic mask. A lift-off resist (Shipley LOR2000) was used to pattern metal pads and interconnects (Ti 10 nm/Pt 150 nm). Exposure was performed using an ASML stepper (ASML PAS 550). For the devices with PEDOT:PSS coatings, a PaC peel-off step to pattern the PEDOT:PSS was used.[56] Impedance measurements of the electrodes were performed *in vitro* using 1× Phosphate Buffer Solution (PBS) and an Ag/AgCl reference wire.

Shuttle microwire preparation and assembly with a guiding system

Microwires were prepared using a technique previously reported.[28] Briefly, a 2M KOH was prepared using dices (Fischer) in deionized water. Tungsten wire (Goodfellow USA) was slid into a 100 μm inner-diameter polyimide tubing (NeuraLynx), leaving several centimeters protruding on each side. Microwires were then electrosharpened using a 2 V DC bias against an Ag/AgCl reference electrode. The protruding length of the microwire was then adjusted, and the other extremity was sealed to the polyimide tubing to prevent sliding of the microwire.

Animal surgery for chronic recordings

All procedures and animal care were approved by the Institutional Animal Care and Use Committee at Stanford University School of Medicine. Two adult Long Evans male rats aged

3–4 months and weighing 400–500 g were used in this study (Charles River Laboratories). In typical procedures, we performed a 2.5 × 2.5 mm^2 craniotomy (−3.6 mm AP and −2.2 mm ML from Bregma) and removed the dura mater. The device mounted into the 3D printed hat was vertically mounted on a micromanipulator (Model 963, Kopf Instruments) and positioned above the craniotomy hole. As the device traveled downward, the protruding tip penetrated the neural tissue. Once the neural probe reached the desired depth and the time of release was achieved, the shuttle microwire was retracted. The exposed surrounding tissue was covered with Kwik-Sil (World Precision Instruments), and the hat was secured to the rodent's skull using standard procedures with initial layers of Metabond and dental cement.

μCT imaging

Three dimensional computerized X-ray tomography images were performed to image NeuroRoots devices with PEDOT:PSS coated electrodes implanted 3 mm deep into a rat brain. Implantation of the NeuroRoots device was performed immediately following the extraction of the brain of a rat using a 100 μm diameter microwire as a shuttle. The sample was then immersed in a fixative solution (2% formaldehyde) for 6 days before imaging. Images were taken using a Zeiss Versa 510 (80 kV excitation voltage and 7 W power). Image processing was done with the associated Zeiss software and care was taken to ensure feature dimensions in the μCT images were consistent with measurements from optical microscopy.

Histological sample preparation

Chronic experiments

Animals were transcardially perfused first with saline, and then with 150 ml of fixative solution containing 4% PFA in 0.1M phosphate buffer (PB). Tissue blocks were cut horizontally on a Vibratome (Leica VT1200S, Leica Microsystems, France) into 40 μm sections after extensive washes in PB, and glial fibrillary acidic protein (GFAP) staining was used [GFAP Monoclonal Antibody (GA5), Alexa Fluor 488, Thermofisher, France]. Sections were mounted on Super-Frost slides and covered with a mounting medium containing 2-(4-amidinophenyl)-1H-indole-6-carboxamidine (DAPI) (Flouromount Mounting Medium with DAPI, Abcam, UK).

Cerebellar slice preparation for physiology experiments

Cerebellar axial sections of 70 μm thickness were made at −15 to 20 °C using a cryostat (Leica CM 1860) and an optimal cutting temperature compound. For cryoprotection, the brain tissue was equilibrated in 30% sucrose solution in 1× PBS at 4 °C prior to sectioning. The slices were collected as free-floating sections in 1× PBS with 0.05% sodium azide and stored at 4 °C.

Data acquisition and processing

Data were collected using either a Digital Lynx SX acquisition system (NeuraLynx, Inc.) or an RHS2000 (Intan Technology). Local field potential signals were collected for the 32 channels and locally amplified with an active headstage device (HS-72-QC, NeuraLynx, Inc.). Signals were sampled at 32 kHz. The headstage further provided positional information through mounted LEDs that were tracked via an overhead camera. Chronic LFPs and APs were recorded either in open field or in a double Y-Maze (1.4 × 1.2 m^2) during normal behavior or trained tasks. The data were analyzed using MATLAB (MathWorks). Spike detection was achieved through the following processing steps: filtering of the data with a bandpass filter set to 600–7000 Hz, Principal Component Analysis (PCA), and k-means clustering. From the threshold analysis of each individual channel, 1 ms events were extracted, centered around each peak. The PCA features were then computed, and the data were projected onto the ten largest components to generate the feature vectors. Subsequently, k-means clustering, an unsupervised learning method, was applied, with k ranging from 2 to 4. Through manual curation, each cluster was consolidated over time. The two largest PCA components of the first recorded date of the cluster were used as the basis vectors. For each date, the cluster points were projected onto the basis vectors, and a multivariate Gaussian distribution was subsequently fitted. We used the Mahalanobis distance of the mean of the distribution of the week 7 to the distribution of week 1 to calculate the variance of the PCA centers. The signal-to-noise ratio (SNR) for each channel was computed by dividing the average spike amplitude by its corresponding noise level. The noise level is estimated as the median ($|V|$)/0.6745.

Cerebellum recordings and analysis

Slice experiments

Mice (~1-month-old C57Bl/6J) were anesthetized using isoflurane (1%–3%), decapitated, and their brains were extracted and sliced in ice-cold artificial cerebrospinal fluid (ACSF bubbled with 95% O_2 and 5% CO_2 to maintain pH at 7.3; osmolality 323 mOsm). Parasagittal cerebellar vermis slices of 400 μm thickness were cut using a VT 1200 Vibratome (Leica) and were incubated in ACSF at 37 °C for 45 min before conducting electrophysiology experiments. NeuroRoots were mounted onto the micromanipulator (Sutter Instruments) and visually guided to the slice by an upright microscope (Zeiss Axioscope 2 fs). The recordings were obtained using a RHS2000 (Intan Technology), and the signals were sampled at 30 kHz.

Acute in vivo cerebellar recording

Prior to surgery, the mice received a subcutaneous injection of carprofen (5–10 mg/kg). Mice were then anesthetized using isoflurane. An incision was made to expose the interparietal and occipital areas of the skull, and a craniotomy (~2 mm in diameter centered ~1.5 mm right of the midline) was performed to expose the cerebellum. Each channel was filtered using a fifth order band pass Butterworth filter with cutoff frequencies of 140 and 2000 Hz. Spike sorting was conducted offline using Plexon Offline Sorter (Plexon Inc.) using template matching in combination with principle component visualization.

SUPPLEMENTARY MATERIAL

The supplementary material encompasses Figure S1: Calculation of bending stiffness of the NeuroRoots compared to a

myelinated axon of 3 μm diameter. To have equivalent bending stiffness, the Neuroroot would need to be 1.3 μm thick, compared to the measured thickness of 1.5 μm. Figure S2: Microscope image of the tip of the PEDOT:PSS version of the NeuroRoots. The inset shows the 100 μm long electrode sites coated with PEDOT:PSS (green/blue color). Figure S3: Electrical impedance of the NeuroRoot electrodes, showing <100 kΩ impedance at 1000 Hz for all devices. Figure S4: Histological evaluation of NeuroRoots along the insertion trajectory. Histological verification of a 90-days-post-implantated, large PEDOT:PSS coated NeuroRoots implanted with a 100 μm diameter microwire. High magnification images show horizontal cross sections of the tissue response around the (i) tip of the implant and in the hippocampus (ii) along the trajectory of the implant in the cortical region above the hippocampus. GFAP staining (green) shows reactive astrocytes 90 days post-implantation, whereas DAPI (blue) labels cell nuclei in the neural tissue. Thin white arrows show tissue reaction (GFAP), whereas bold white arrow show the pyramidal layer of the hippocampus. Scale bar: 100 μm. Figure S5: Principal Component Analysis of one electrode cluster for a chronic *in vivo* experiment. The dots are the centers of the principal components. Ovals are the 2σ contour of the PC distribution. Colors code the time stamps the data were extracted from. Each color is representative of recordings from a different week, as described in the colored legend of Fig. 3. Figure S6: Principal Component Analysis of the cerebellum units that were shown in Fig. 4(d).

ACKNOWLEDGMENTS

The authors thank A. Obaid (Stanford University), D. Khodagholy and J. N. Gelinas (Columbia University) for fruitful discussions. They also thank Makoto Nakamura from ASML and the Stanford Nanofabrication Facility (SNF) for help with the device fabrication, Sawson Taheri from the Stanford Prototyping Facility (SPF) for their help with the PCB design, Quentin Payan from WurthElektronik for the ZIF connectors, and the Biosphera team for the original rat 3D model used in Fig. 2(b). They thank Damiano Barone and Anthony Dennis, respectively, for assistance with μCT sample preparation and μCT imaging.

M.F. was supported by U.S. National Institutes of Health Grants (Grant Nos. 1R21EY026365-01 and R21NS104861 from NIH/NINDS) and the Stanford Wu Tsai Institute "Neuro science:Translate". Part of this work was performed at the Stanford Nanofabrication Facilities (SNF) and Stanford Nano Shared Facilities (SNSF), supported by the National Science Foundation under Award No. ECCS-1542152. C.M.P. acknowledges funding from a Whitaker International Scholar Grant administered by the U.S. Institute for International Education as well as funding from the University of Cambridge Borysiewicz Biomedical Fellowship program. G.G.M. and C.M.P. acknowledge funding from the European Union's Horizon 2020 Research and Innovation Program under Grant Agreement No. 732032 (BrainCom). L.G. is a New York Stem Cell Foundation – Robertson Investigator, supported by funding from The New York Stem Cell Foundation, the James S. McDonnell Foundation, Grant No. NIMH MH106475, and the Simons Foundation. J.R. acknowledges funding from Simons Foundation Grant Nos. 543031, NIH R01 DC004154, and R01 NS072406. A.W. and A.S. acknowledge funding from the European Research Council (ERC) under the European Union's Horizon 2020 research and innovation program (Grant Agreement No. 716867) as well as Excellence Initiative of Aix-Marseille University - A*MIDEX, a French "Investissements d'Avenir" program. A.W., M.J.D., and A.S. were additionally supported by the Ministry of Human Capacities, Hungary (Grant No. 20391-3/2018/FEKUSTRAT).

AUTHOR DECLARATIONS

Conflict of Interest

The authors have no conflicts to disclose.

Author Contributions

M.D.F. and C.M.P. contributed equally to this work.

M.D.F. and C.M.P. were primary experimental contributors. M.D.F., C.M.P., G.G.M. and N.A.M. conceived the basic device concept and designed the experiments. M.D.F. designed and fabricated the devices and platform for the chronic recording experiments. A.G. and M.D.F. recorded the chronic signals and M.D.F., A.G., and E.Z. analyzed the data. M.D.F., S.J., and M.G. recorded and analyzed the cerebellar data. M.D.F., S.J., and M.G. recorded and analyzed the cerebellar data. C.M.P., M.D.F., J.P., G.D., M.J.D., fabricated and characterized the devices for acute and histology experiments. A.S. performed histology preparation and imaging. M.D.F. and N.A.M. wrote the manuscript. All authors reviewed the manuscript and provided comments.

Marc D. Ferro: Conceptualization (equal); Data curation (lead); Writing – original draft (equal). **Christopher M. Proctor**: Conceptualization (equal); Data curation (equal); Methodology (lead); Writing – original draft (equal); Writing – review & editing (equal). **Alexander Gonzalez**: Data curation (equal); Methodology (equal); Writing – review & editing (equal). **Sriram Jayabal**: Data curation (equal); Methodology (equal); Writing – review & editing (equal). **Eric Zhao**: Data curation (equal); Methodology (equal); Writing – review & editing (equal). **Maxwell Gagnon**: Data curation (equal); Methodology (equal); Writing – review & editing (equal). **Andrea Slézia**: Data curation (equal); Methodology (equal); Writing – review & editing (equal). **Jolien Pas**: Data curation (equal); Methodology (equal); Writing – review & editing (equal). **Gerwin Dijk**: Data curation (equal); Methodology (equal); Writing – review & editing (equal). **Mary J. Donahue**: Methodology (equal); Writing – review & editing (equal). **Adam Williamson**: Funding acquisition (equal); Writing – review & editing (equal). **Jennifer Raymond**: Funding acquisition (equal); Writing – review & editing (equal). **George G. Malliaras**: Conceptualization (equal); Funding acquisition (equal); Writing – review & editing (equal). **Lisa Giocomo**: Resources (equal); Writing – review & editing (equal). **Nicholas A. Melosh**: Conceptualization (equal); Funding acquisition (equal); Investigation (equal); Resources (equal); Writing – review & editing (equal).

DATA AVAILABILITY

The data that support the findings of this study are available within the article and its supplementary material. Additional data

related to this paper may be requested from the corresponding author upon reasonable request.

REFERENCES

[1] D. Khodagholy *et al.*, "Organic electronics for high-resolution electrocorticography of the human brain," Sci. Adv. **2**, e1601027 (2016).
[2] D. Khodagholy *et al.*, "NeuroGrid: Recording action potentials from the surface of the brain," Nat. Neurosci. **18**, 310–315 (2015).
[3] I. R. Minev *et al.*, "Electronic dura mater for long-term multimodal neural interfaces," Science **347**, 159–163 (2015).
[4] J. D. Loudin *et al.*, "Optoelectronic retinal prosthesis: System design and performance," J. Neural Eng. **4**, S72 (2007).
[5] H. S. Mayberg *et al.*, "Deep brain stimulation for treatment-resistant depression," Neuron **45**, 651–660 (2005).
[6] J. M. Bronstein *et al.*, "Deep brain stimulation for Parkinson disease: An expert consensus and review of key issues," Arch. Neurol. **68**, 165 (2011).
[7] G. Santhanam, S. I. Ryu, B. M. Yu, A. Afshar, and K. V. Shenoy, "A high-performance brain–computer interface," Nature **442**, 195–198 (2006).
[8] L. R. Hochberg *et al.*, "Neuronal ensemble control of prosthetic devices by a human with tetraplegia," Nature **442**, 164–171 (2006).
[9] T. Milekovic *et al.*, "Stable long-term BCI-enabled communication in ALS and locked-in syndrome using LFP signals," J. Neurophysiol. **120**, 343 (2018).
[10] J. Rivnay, H. Wang, L. Fenno, K. Deisseroth, and G. G. Malliaras, "Next-generation probes, particles, and proteins for neural interfacing," Sci. Adv. **3**, e1601649 (2017).
[11] R. Chen, A. Canales, and P. Anikeeva, "Neural recording and modulation technologies," Nat. Rev. Mater. **2**, 16093 (2017).
[12] G. Hong and C. M. Lieber, "Novel electrode technologies for neural recordings," Nat. Rev. Neurosci. **20**, 330–345 (2019).
[13] L. Wang *et al.*, "Recent advances in implantable neural interfaces for multimodal electrical neuromodulation," Adv. Healthcare Mater. 2303316 (2024) (published online).
[14] L. Luan *et al.*, "Ultraflexible nanoelectronic probes form reliable, glial scar–free neural integration," Sci. Adv. **3**, e1601966 (2017).
[15] G. Hong, X. Yang, T. Zhou, and C. M. Lieber, "Mesh electronics: A new paradigm for tissue-like brain probes," Curr. Opin. Neurobiol. **50**, 33–41 (2018).
[16] T.-M. Fu *et al.*, "Stable long-term chronic brain mapping at the single-neuron level," Nat. Methods **13**, 875–882 (2016).
[17] S. Zhao *et al.*, "Tracking neural activity from the same cells during the entire adult life of mice," Nat. Neurosci. **26**, 696–710 (2023).
[18] D. Khodagholy *et al.*, "High transconductance organic electrochemical transistors," Nat. Commun. **4**, 2133 (2013).
[19] J.-W. Jeong *et al.*, "Soft materials in neuroengineering for hard problems in neuroscience," Neuron **86**, 175–186 (2015).
[20] K. J. Seo *et al.*, "A soft, high-density neuroelectronic array," npj Flexible Electron. **7**, 40 (2023).
[21] T. Someya, Z. Bao, and G. G. Malliaras, "The rise of plastic bioelectronics," Nature **540**, 379–385 (2016).
[22] J. J. Jun *et al.*, "Fully integrated silicon probes for high-density recording of neural activity," Nature **551**, 232–236 (2017).
[23] B. C. Raducanu *et al.*, "Time multiplexed active neural probe with 1356 parallel recording sites," Sensors **17**, 2388 (2017).
[24] Z. Zhao *et al.*, "Ultraflexible electrode arrays for months-long high-density electrophysiological mapping of thousands of neurons in rodents," Nat. Biomed. Eng. **7**, 520–532 (2022).
[25] E. Musk and Neuralink, "An integrated brain-machine interface platform with thousands of channels," J. Med. Internet Res. **21**, e16194 (2019).
[26] D. Liewald, R. Miller, N. Logothetis, H.-J. Wagner, and A. Schüz, "Distribution of axon diameters in cortical white matter: An electron-microscopic study on three human brains and a macaque," Biol. Cybern. **108**, 541–557 (2014).
[27] H. Ouyang, E. Nauman, and R. Shi, "Contribution of cytoskeletal elements to the axonal mechanical properties," J. Biol. Eng. **7**, 21 (2013).
[28] A. Obaid, Y. W. Wu, M. Hanna, W. Nix, J. Ding, N. A. Melosh *et al.*, "Ultra-sensitive measurement of brain penetration with microscale probes for brain machine interface considerations," bioRxiv (2018).
[29] E. M. Callaway and A. K. Garg, "Brain technology: Neurons recorded en masse," Nature **551**, 172–173 (2017).
[30] K. D. Harris, D. A. Henze, J. Csicsvari, H. Hirase, and G. Buzsáki, "Accuracy of tetrode spike separation as determined by simultaneous intracellular and extracellular measurements," J. Neurophysiol. **84**, 401–414 (2000).
[31] A. Marques-Smith *et al.*, "Recording from the same neuron with high-density CMOS probes and patch-clamp: A ground-truth dataset and an experiment in collaboration," bioRxiv (2018).
[32] M. D. Ferro and N. A. Melosh, "Electronic and ionic materials for neurointerfaces," Adv. Funct. Mater. **28**, 1704335 (2018).
[33] S. Felix *et al.*, "Removable silicon insertion stiffeners for neural probes using polyethylene glycol as a biodissolvable adhesive," in *2012 Annual International Conference of the IEEE Engineering in Medicine and Biology Society* (IEEE, 2012), pp. 871–874.
[34] J. Pas *et al.*, "A bilayered PVA/PLGA-bioresorbable shuttle to improve the implantation of flexible neural probes," J. Neural Eng. **15**, 065001 (2018).
[35] A. Lecomte *et al.*, "Silk and PEG as means to stiffen a parylene probe for insertion in the brain: Toward a double time-scale tool for local drug delivery," J. Micromech. Microeng. **25**, 125003 (2015).
[36] Z. J. Du *et al.*, "Ultrasoft microwire neural electrodes improve chronic tissue integration," Acta Biomater. **53**, 46–58 (2017).
[37] T. D. Y. Kozai *et al.*, "Ultrasmall implantable composite microelectrodes with bioactive surfaces for chronic neural interfaces," Nat. Mater. **11**, 1065–1073 (2012).
[38] C. P. Tan and H. G. Craighead, "Surface engineering and patterning using parylene for biological applications," Materials **3**, 1803–1832 (2010).
[39] K. T. Shimizu, J. D. Fabbri, J. J. Jelincic, and N. A. Melosh, "Soft deposition of large-area metal contacts for molecular electronics," Adv. Mater. **18**, 1499–1504 (2006).
[40] J. C. Barrese, J. Aceros, and J. P. Donoghue, "Scanning electron microscopy of chronically implanted intracortical microelectrode arrays in non-human primates," J. Neural Eng. **13**, 026003 (2016).
[41] See http://neuronexus.com/catalogs-brochures/ for Catalogs NeuroNexus.
[42] J. W. Salatino, K. A. Ludwig, T. D. Y. Kozai, and E. K. Purcell, "Glial responses to implanted electrodes in the brain," Nat. Biomed. Eng. **1**, 862 (2017).
[43] J. C. Barrese *et al.*, "Failure mode analysis of silicon-based intracortical microelectrode arrays in non-human primates," J. Neural Eng. **10**, 066014 (2013).
[44] I. Terem *et al.*, "Revealing sub-voxel motions of brain tissue using phase-based amplified MRI (aMRI)," Magn. Reson. Med. **80**, 2549 (2018).
[45] B. S. McEwen, "Stress, sex, and neural adaptation to a changing environment: Mechanisms of neuronal remodeling," Ann. N. Y. Acad. Sci. **1204**, E38–E59 (2010).
[46] M. Glickstein, "What does the cerebellum really do?," Curr. Biol. **17**, R824–R827 (2007).
[47] A. Katoh, S.-L. Shin, R. R. Kimpo, J. M. Rinaldi, and J. L. Raymond, "Purkinje cell responses during visually and vestibularly driven smooth eye movements in mice," Brain Behav. **5**, e00310 (2015).
[48] C. Schwarz and J. P. Welsh, "Dynamic modulation of mossy fiber system throughput by inferior olive synchrony: A multielectrode study of cerebellar cortex activated by motor cortex," J. Neurophysiol. **86**, 2489–2504 (2001).
[49] H. E. Halverson, A. Poremba, and J. H. Freeman, "Medial auditory thalamus is necessary for acquisition and retention of eyeblink conditioning to cochlear nucleus stimulation," Learn. Mem. **22**, 258–266 (2015).
[50] S. P. Marshall, R. S. Van Der Giessen, C. I. De Zeeuw, and E. J. Lang, "Altered olivocerebellar activity patterns in the connexin36 knockout mouse," Cerebellum **6**, 287–299 (2007).

[51]M. J. Wagner, T. H. Kim, J. Savall, M. J. Schnitzer, and L. Luo, "Cerebellar granule cells encode the expectation of reward," Nature **544**, 96–100 (2017).
[52]B. Deverett, S. A. Koay, M. Oostland, and S. S.-H. Wang, "Cerebellar involvement in an evidence-accumulation decision-making task," eLife **7**, e36781 (2018).
[53]F. Najafi, A. Giovannucci, S. S.-H. Wang, and J. F. Medina, "Coding of stimulus strength via analog calcium signals in Purkinje cell dendrites of awake mice," eLife **3**, e03663 (2014).
[54]M. A. Gaffield, S. B. Amat, H. Bito, and J. M. Christie, "Chronic imaging of movement-related Purkinje cell calcium activity in awake behaving mice," J. Neurophysiol. **115**, 413–422 (2016).
[55]D. Kostadinov, M. Beau, M. B. Pozo, and M. Häusser, "Predictive and reactive reward signals conveyed by climbing fiber inputs to cerebellar Purkinje cells," Nat. Neurosci. **22**, 950–962 (2019).
[56]A. Williamson *et al.*, "Localized neuron stimulation with organic electrochemical transistors on delaminating depth probes," Adv. Mater. **27**, 4405–4410 (2015).